

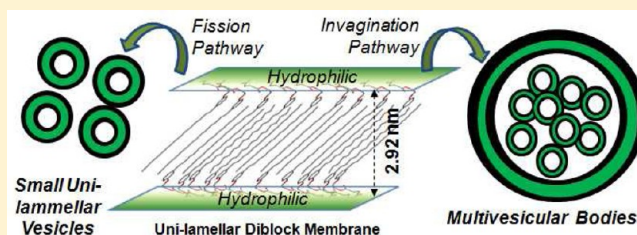
# Amphiphilic Diblocks Sorting into Multivesicular Bodies and Their Fluorophore Encapsulation Capabilities

Smita Kashyap and M. Jayakannan\*

Department of Chemistry, Indian Institute of Science Education and Research (IISER)-Pune, Dr. Homi Bhabha Road, Pune 411008, Maharashtra, India

## Supporting Information

**ABSTRACT:** Synthetic macromolecular diblocks sorting into multivesicular bodies (MVBs) and their fluorophore encapsulation pathways were reported. Renewable resource based diblocks having hydrophobic units and flexible hydrophilic polyethylene glycols (PEG) were custom designed for the above purpose. Single crystal structure was resolved to prove the existence of the strong intermolecular interactions and the formation of unilamellar layer-like self-assemblies. These amphiphilic AB diblocks underwent selective vesicular fission either by outward budding or inward invagination to produce small unilamellar vesicles (SUVs) or MVBs, respectively. Self-organization parameters such as relative volume ( $\nu_e$ ) and reduced area difference ( $\Delta a_0$ ) were determined on the basis of theoretical models, and very good correlation with the experimental results was established for the synthetic-MVBs. Pyrene was encapsulated to study the mechanistic aspects of the MVB formations. An unusual nonlinear trend was observed in the pyrene dynamic excimer formation with respect to the sorting of diblock membrane into MVBs. Strong intermolecular interaction was found to be a critical deciding factor in synthetic diblock membranes to facilitate MVBs. The approach demonstrated here opens up new design strategies for biomimicking of MVBs in synthetic macromolecules which are potential vectors for drug delivery.



## INTRODUCTION

Multivesicular bodies (MVBs) are very important key intermediates in the regulation of several physiological processes under tightly controlled signaling pathways across the biological cell membranes.<sup>1,2</sup> MVBs are formed in the biogenesis of the liposomal organelles in which portions of the diblock membrane invaginate into small intraluminal vesicles (ILVs) and subsequently are released into the lumen.<sup>3</sup> MVBs are identified to play a crucial role as cargo-transport machinery via a complicated multistep process in the functioning of human immunodeficiency virus (HIVs) and down regulation of receptors and transporters in enveloped viruses of plasma membranes.<sup>4,5</sup> Though the evolution of MVBs *in vivo* is still under debate, recent *in vitro* studies revealed that the ubiquitin directed endosomal sorting complex responsible for transport (ESCRT) protein accounts for these unusual cell machineries.<sup>6,7</sup> The ILVs produced by the sorting of diblock membrane have unique advantages in that these small internal vesicles were perfectly protected by the sorting membrane; as a result, these nano-objects were less susceptible to external stimuli such as pH and temperature, etc.<sup>8</sup> Therefore, MVBs behave as storage vesicles of cargo (drug/gene) which have to be delivered to the internal part of the animal cells. Synthetic macromolecule based vesicular self-assemblies were reported in single-component and multicomponent phospholipids, metal ion–amphiphilic ligand interactions, charge-transfer complexes, light-responsive guest–host complexes, dendritic and hyperbranched polymers, and so on.<sup>9</sup> Despite significant advances

made in producing small unilamellar vesicles (SUVs),<sup>10</sup> giant unilamellar vesicles (GUVs),<sup>11</sup> and multilamellar vesicles (MLVs)<sup>12</sup> in liposome and synthetic macromolecules,<sup>13</sup> mimicking of synthetic MVBs is far from reality. Biomimicking of MVBs in synthetic vesicles is an important task<sup>14</sup> which could further fuel the creation of complex membrane models and their encapsulation capabilities resembling cell membranes which have potential applications in the chemistry–biology interface.

The present investigation is emphasized on mimicking of multivesicular bodies (MVBs) in bioinspired synthetic AB diblock membranes. Custom designed renewable resource based amphiphilic AB-diblocks formed unilamellar structures in water, and they subsequently self-organized either as SUVs or MVBs depending upon their hydrophilic content (see Figure 1). Single crystal structure was resolved for the amphiphilic building blocks to confirm the origin of unilamellar packing in the vesicular structures. Further, theoretical calculations were performed to determine two important structural parameters: reduced volume ( $\nu_e$ ) and reduced area difference ( $\Delta a_0$ ) of the synthetic diblock membrane. A direct correlation between theoretical calculation and experimental results was achieved, and it was found that inward invagination and outward budding of diblock membranes exclusively produced MVBs or SUVs, respectively. Additionally, the mechanistic aspect of MVB

Received: April 29, 2012

Revised: July 16, 2012

Published: July 17, 2012

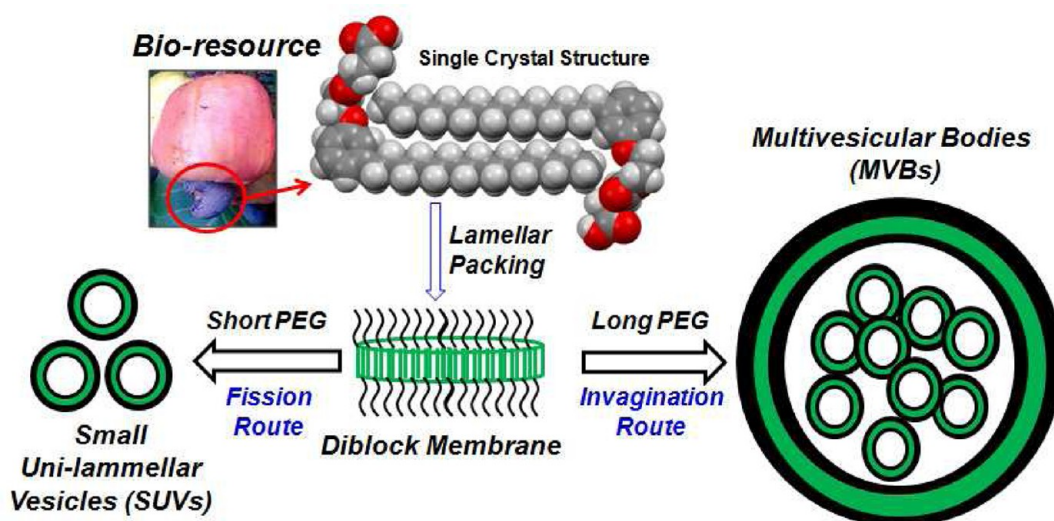
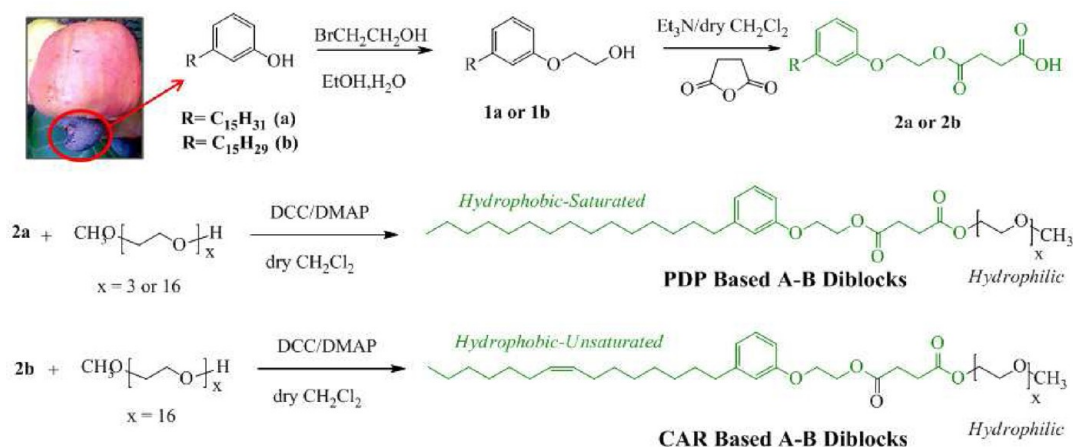


Figure 1. Synthetic diblock membranes sorting into MVBs and SUVs.

Scheme 1. Synthesis of Renewable Resource Based AB Diblocks



formation was studied using pyrene encapsulation in water. The detailed photophysical experiments revealed that the diblock membranes showed an unusual nonlinear trend in the excimer formation with their self-organization in water. MVB formation was facilitated by the strong intermolecular interactions in the membrane. The present investigation opens up a new concept of biomimicking MVBs in synthetic vesicles, more specifically, bioresource based amphiphilic AB diblocks.

## RESULTS AND DISCUSSION

Two naturally available plant based long tailed phenolic compounds such as cardanol (contains  $\omega$ -unsaturated alkyl chain) and its saturated analogue 3-pentadecylphenol were chosen as the hydrophobic units for the AB diblock design (see Scheme 1). Both cardanol and 3-pentadecylphenol are the main constituents of cashew nut shell liquid which are produced as plant based industrial waste. 3-Pentadecylphenol was reacted with 2-bromoethanol in the presence of NaOH as a base to give 2-(3-pentadecylphenoxy)ethanol (**1a**). Succinic anhydride was ring opened with **1a** in the presence of Et<sub>3</sub>N as a base to give 4-oxo-4-(2-(3-pentadecylphenoxy)ethoxy)butanoic acid (**2a**). The compound **2a** was further coupled with triethylene glycol monomethyl ether (TEG) and polyethylene glycol (PEG-750) monomethyl ether to produce two A–B diblocks

PDP-TEG and PDP-PEG-750, respectively (PDP represents pentadecylphenol as the hydrophobic part). Cardanol was converted into **2b** (as described for **2a**) and reacted with PEG-750 monomethyl ether to obtain CAR-PEG-750 diblock (CAR represents cardanol as the hydrophobic part). The diblocks were purified (by column chromatography and dialysis using a semipermeable membrane), and their structures were characterized by <sup>1</sup>H, <sup>13</sup>C NMR, and MALDI-TOF (see the Supporting Information). All three blocks showed a monomodal distribution in GPC chromatogram (see SF-1, Supporting Information) with a narrow polydispersity of 1.02. The higher molecular weight long PEG-lated diblocks PDP-PEG-750 and CAR-PEG-750 were found to have a lower retention time than that of PDP-TEG due to their higher molecular weights. Among the long PEG-lated diblocks, the saturated tailed (PDP-PEG-750) had little lower retention time compared to its unsaturated counterpart (CAR-PEG-750 diblock). This trend was attributed to the higher hydrodynamic radius of the diblocks in solvent (in THF) by the more compact saturated hydrophobic tails compared to the flexible partially unsaturated ones.

The current molecular design provides two categories of A–B diblocks to study their self-assembly in water: (i) fixed hydrophobic

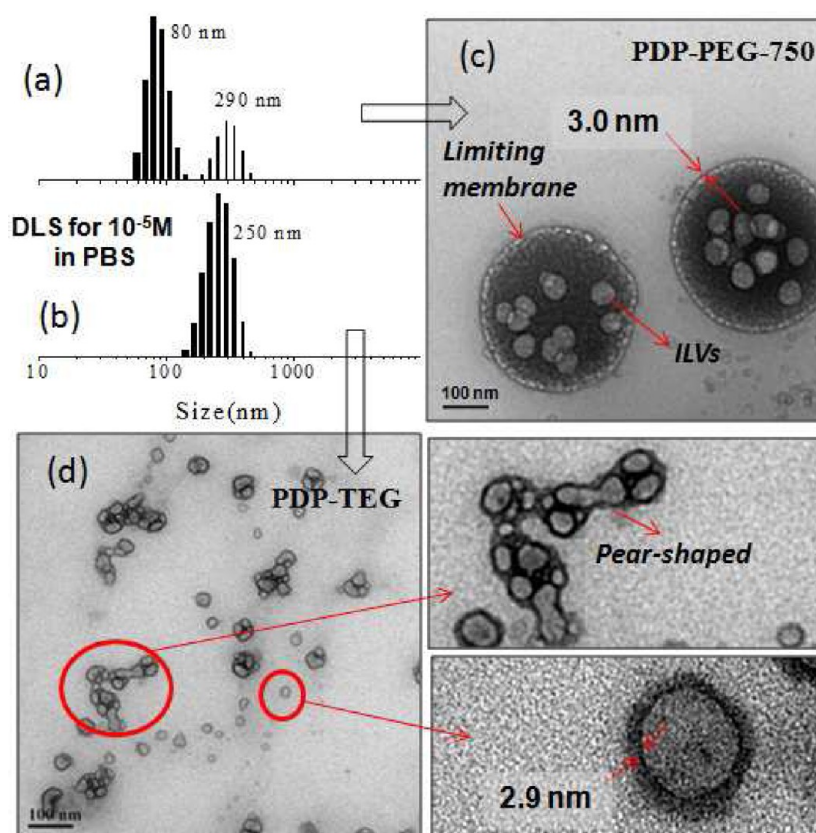


**Figure 2.** DLS histograms of AB diblocks in PDP-PEG-750 (a) and PDP-TEG (b) in PBS at  $10^{-5}$  M. HR-TEM images of PDP-PEG-750 (c) and PDP-TEG (d).

units (PDP alkyl units) with variable hydrophilic PEG chain lengths (PDP-TEG and PDP-PEG-750) and (ii) variable hydrophobic units (PDP and CAR) with fixed hydrophilic PEG-750 chains (PDP-PEG-750 and CAR-PEG-750). To determine the self-assembled structures formed by the A–B diblocks, the aqueous solution of the samples was subjected to dynamic light scattering (DLS) analysis. DLS histograms recorded for PDP-PEG-750 and PDP-TEG blocks in PBS (phosphate buffer saline, pH 7.4) at  $1 \times 10^{-5}$  M are shown in Figure 2a and b, respectively. PDP-PEG-750 showed a broad distribution with the formation of aggregates with sizes ranging from 80 to 300 nm. PDP-TEG showed a narrow distribution with the formation of uniform size aggregates of 200–250 nm in water. The formation of these nanosized aggregates may be explained on the basis of hydrophilic–hydrophobic interaction between the molecules as they come close together in water. These nanoaggregates were found to be stable under longer storage (5 days) and at both acidic to neutral pH (see Figure SF2, Supporting Information). To visualize the size and shape of the A–B diblock nanoaggregates, the samples were subjected to high resolution transmission electron microscope (TEM) analysis. HR-TEM images of PDP-PEG750 and PDP-TEG are given in Figure 2c and d. The morphology of PDP-PEG750 was found to be identical to multivesicular bodies (MVBs) consisting of spherical shaped diblock membrane which accommodated  $10 \pm 4$  intraluminal vesicles (ILVs) of  $\sim 45$ –50 nm in diameter (see SF3, Supporting Information, for more images). Both the diblock membrane and ILVs were found to have identical wall thicknesses ( $\sim 3.0$  nm) which further supported the sorting of ILVs from the same diblock membrane.

The enlarged portion of the PDP-PEG-750 vesicles clearly showed the appearance of a dark hydrophobic layer covered by

a hydrophilic corona at the outer surface (see SF3, Supporting Information). On the other hand, the PDP-TEG block with short hydrophilic PEG chain showed the formation of isolated small unilamellar vesicles (SUVs) of 40 nm diameter with wall thickness  $\sim 2.9$  nm. The enlarged section of Figure 2d confirmed the existence of SUVs as aggregated compound vesicles. This is in confirmation with the existence of large aggregates for PDP-TEG observed in the DLS data (Figure 2b).<sup>15</sup> Further, images of pear-shaped vesicles which were yet to be split into individual SUVs were also clearly visible in Figure 2d (see also SF-4, Supporting Information). Atomic force microscopic analysis of the diblocks confirmed the spherical shape of the vesicles, and the size of the vesicles matched with that of TEM (see SF-5, Supporting Information). The unsaturated hydrophobic block CAR-PEG-750 did not show any self-organization in water; as a result, no definite morphology was observed (see SF-6, Supporting Information). Hence, both the nature of the hydrophobic units (saturated or unsaturated chain) and length of the PEG chain played a crucial role in the molecular self-assembly of A–B diblocks in water.

The packing of surfactant molecules into self-assembled objects like lamellar arrangements was typically validated by using their single crystal structures. Unfortunately, most of the surfactant molecules are typically liquids or low melting solids and it is very difficult to obtain single crystal data to trace their molecular interactions. Recently, Smith et al. had successfully grown single crystals for sodium dodecyl sulfate and established the correlation between the molecular packing with its unilamellar self-organization.<sup>16</sup> However, crystallographic evidence for the micelle or vesicular packing of amphiphiles is very rare in the literature. In order to understand the nature of the chain



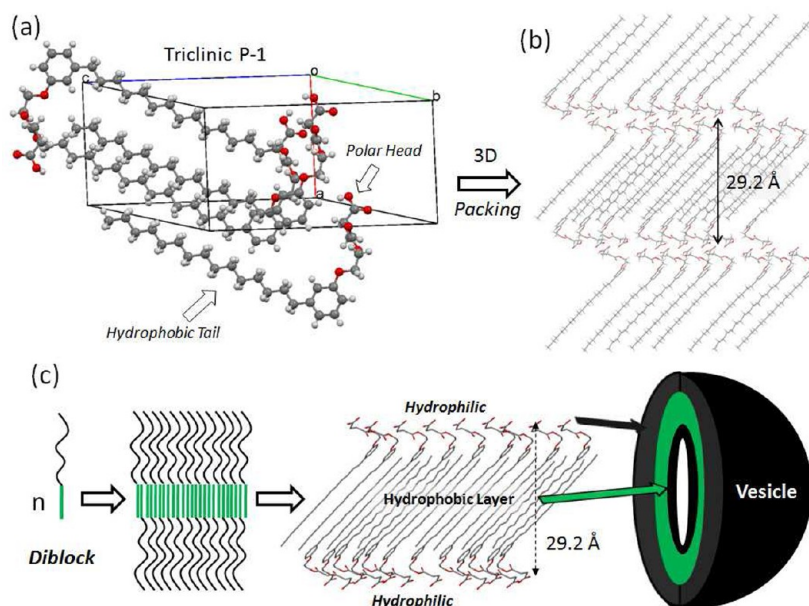


**Figure 3.** Single crystal structure of compound **2a**. Unit cell (a) and the three-dimensional packing of molecules along the *a*-axis (b). The packing diagram represents the unilamellar formation and its spherical vesicle (c).

packing in the present vesicular structures, the single crystal X-ray structure of the hydrophobic PDP unit was resolved. A–B diblocks were liquid-like in nature and did not form crystals. Interestingly, good quality single crystals were grown for their synthetic intermediate compound **2a** (see Scheme 1) in dichloromethane/methanol solvent mixture (2:3 v/v). The molecule **2a** has the same features of the hydrophobic part as in the AB blocks, and therefore, it could be presumed that its crystal structure could provide direct information on the packing of PDP units in the vesicle. The single crystal X-ray structure of **2a** is shown in Figure 3, and other details are given in the Supporting Information (SF-7, SF-8, and ST1). The molecule **2a** crystallized in triclinic lattice in the space group of P-1, and their unit cell parameters were determined as  $a = 10.795$ ,  $b = 20.28$ ,  $c = 24.74$ ,  $\alpha = 85.30$ ,  $\beta = 85.82$ , and  $\gamma = 75.68$  with an *R*-factor of 9.43. The pentadecyl chains in the molecule **2a** were organized in all-trans conformations which were separated from the hydrophobic carboxylic functional group (to which PEG chains were connected in the AB diblocks). The three-dimensional packing of the molecules along the *a*-axis showed the perfect lamellar sheet formation. The alkyl chains were projected toward each other via like interactions and interdigitated to form a hydrophobic layer of thickness 29.2 Å (or 2.92 nm, see Figure 3). The wall thicknesses of the vesicles in SUVs and MVBs were ( $\sim 3.00$  nm, from TEM images) almost identical to the interdigitized hydrophobic layer distance ( $\sim 2.92$  nm, from the crystal structure), indicating that the thin hydrophobic walls in the vesicles were constituted by long tails in the PDP units. On the basis of the crystal packing, it may be concluded that the vesicles (MVBs and SUVs) were typically unilamellar in nature. This is for the first time that such a good correlation has been established between the wall thicknesses of the vesicles and their chemical structure using single crystal analysis. It is very important to mention that the formation of lamellar structures in the vesicular assemblies was elucidated on the basis of two independent techniques like single crystal structure and the morphological analysis by HR-TEM. However, more experimental and theoretical studies are required to confirm the exact packing of hydrophobic structure of the

vesicular model. The identical wall thicknesses of the SUVs or MVBs suggested that the AB diblocks initially would have undergone similar self-organization in water to produce diblock membranes of the same thickness; at later stages, their budding patterns could have varied for the formation of MVBs or SUVs.

On the basis of the theoretical model,<sup>17</sup> the evolution of vesicles was involved in two consecutive steps: (i) AB diblock with hydrophilic and hydrophobic unit undergo self-organization in water to produce a disk-like large diblock membrane with a radius of  $R_D$  and (ii) in order to minimize the membrane-elastic strain energy, these diblock membranes undergo closure to produce larger vesicles of radius  $R_m$  (where  $R_m = R_D/2$ ).<sup>17a</sup> The schematic representation of the vesicle formation is shown in Figure 4. More often, these large vesicles further undergo shape change to reduce the bending energy; as a result, the mother vesicles deformed into either pear-shaped vesicle or stomatocyte with respect to their inward or outward curvatures, respectively.<sup>17b</sup> Two important parameters determine the nature of the curvature, and they are reduced volume ( $\nu$ ) and reduced area difference ( $\Delta a_0$ ) which are defined as

$$\nu = V/[4/3\pi R_m^3] \quad (1)$$

and

$$\Delta a_0 = \Delta A/[8\pi D R_m] \quad (2)$$

where  $V$  is the volume of the vesicle,  $D$  is the bilayer thickness, and  $\Delta A = 2DM$ , where  $M$  is the mean curvature of the vesicle. The reduced volume  $\nu$  and  $\Delta a_0$  are kept at maximum (equal to 1) which corresponds to the most stable spherical shape of vesicles.<sup>17c</sup> The value of  $\Delta a_0 > 1$  and  $\Delta a_0 < 1$  represents the outward and inward curvature of the mother vesicle, respectively. In the event these deformed mother vesicles (stomatocyte or pear-shaped) underwent further transformation into smaller vesicles, the  $\nu$  is replaced by relative volume<sup>17d</sup>  $\nu_e$ , which is represented as

$$\nu_e = \frac{1}{2}[\Delta a_0[3 - (\Delta a_0)^2]] \quad (3)$$

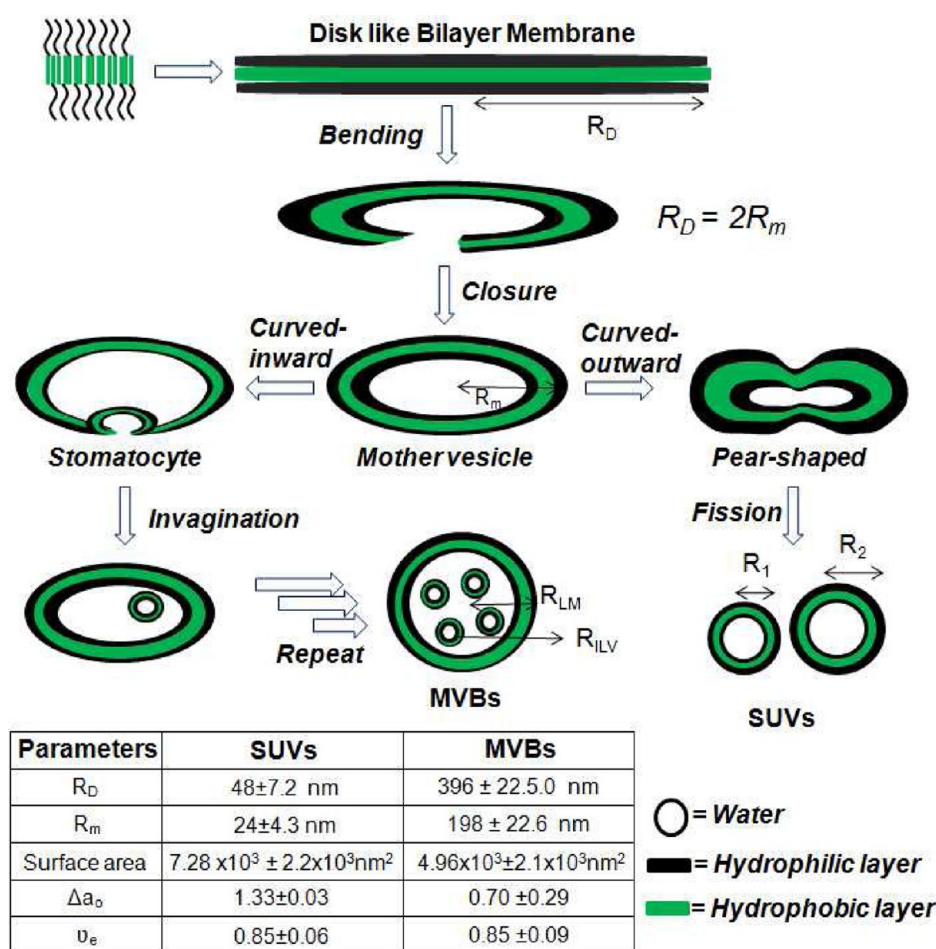


**Figure 4.** Evolution of MVBs and SUVs from diblock membrane and their structural parameters determined on the basis of the theoretical model.

In the case of SUV formation via membrane fission from pear-shaped vesicle, the mean curvature is represented as  $M = 4\pi(R_1 + R_2)$ , where  $R_1$  and  $R_2$  are the radii of the SUVs. Substituting  $M$  in eq 2 results in  $\Delta a = [R_1 + R_2]/R_m$ . In the case of inward invagination and subsequent splitting from the diblock membrane (for MVB formation), the mean curvature became  $M = 4\pi(R_1 - R_2)$ . Substituting  $M$  in this case in eq 2 results in  $\Delta a = [R_1 - R_2]/R_m$  for the generation of intraluminal vesicle in MVBs. On the basis of these theoretical models,  $\nu_e$  and  $\Delta a_0$  were determined for PDP-TEG and PDP-PEG-750 blocks and their values are shown in the table in Figure 4 (see the Supporting Information for a detailed calculation). The radii of the mother vesicle ( $R_m$ ) and the disk-like diblock membrane bilayer ( $R_D$ ) were calculated from the surface area of the SUVs or MVBs, and the values are summarized in the table in Figure 4 (see the Supporting Information for detailed calculations). The  $\nu_e$  values were found to be almost similar in both PDP-TEG ( $0.85 \pm 0.06$ ) and PDP-PEG-750 blocks ( $0.85 \pm 0.09$ ), which indicated that the extent of bilayer closure to spherical mother vesicles was almost identical in both blocks.<sup>17b,c</sup> On the other hand,  $\Delta a_0$  were obtained differently as  $0.70 \pm 0.29$  and  $1.33 \pm 0.03$  for PDP-PEG-750 and PDP-TEG, respectively. For PDP-TEG, the larger  $\Delta a_0$  values ( $>1$ ) confirmed the outward budding of membrane into pear-shaped deformed vesicles (as shown in Figures 2d and 4). The lower  $\Delta a_0$  ( $<1$ ) values supported the deformation of diblock membrane into stomatocyte in the PDP-PEG-750 block (see Figure 4). The inward invagination of stomatocyte in PDP-PEG-750

(see Figure 2c) produced MVBs in synthetic-diblock membrane, as observed in biological cells.

The comparison of  $R_D$  (or  $R_m$ ) values among the AB diblocks indicated that the size of the self-organized bilayer (or mother vesicle) produced by the short hydrophilic block (PDP-TEG) was 1/8 times smaller compared to that of its long PEG chain counterpart PDP-PEG-750. Further, the ratio of the surface area between the large diblock membrane vesicle ( $4\pi R_{LD}$ , which accommodated the small vesicles) and the intraluminal vesicles ( $\sum 4\pi R_i$ ) was calculated. The ratio was obtained as 3:1 (see table in Figure 4), which indicated that, during the multivesicular body formation, the diblock membrane underwent inward invagination up to 25% of its original surface area until it formed a stable spherical vesicle. The repetitive invagination (more than 10 times, as seen in the present case) produced MVBs which were only possible if the stability of the unilamellar diblock membrane was very high in water. To test the packing abilities of AB diblocks, they were subjected to differential scanning calorimetric analysis (DSC) (see SF-9, Supporting Information). The enthalpies of the crystallization and melting transitions (kJ/mol) of the AB block having long PEG-750 units were obtained almost 3–4 times higher than that of its short triethylene glycol counterpart (see ST2, Supporting Information). Typically, strongly packed chains showed higher crystallinity and needed higher energy for melting and released more heat during crystallization. Hence, it can be confirmed that the longer PEG chain facilitated a higher order of packing in the AB diblocks. Further, it was very clear



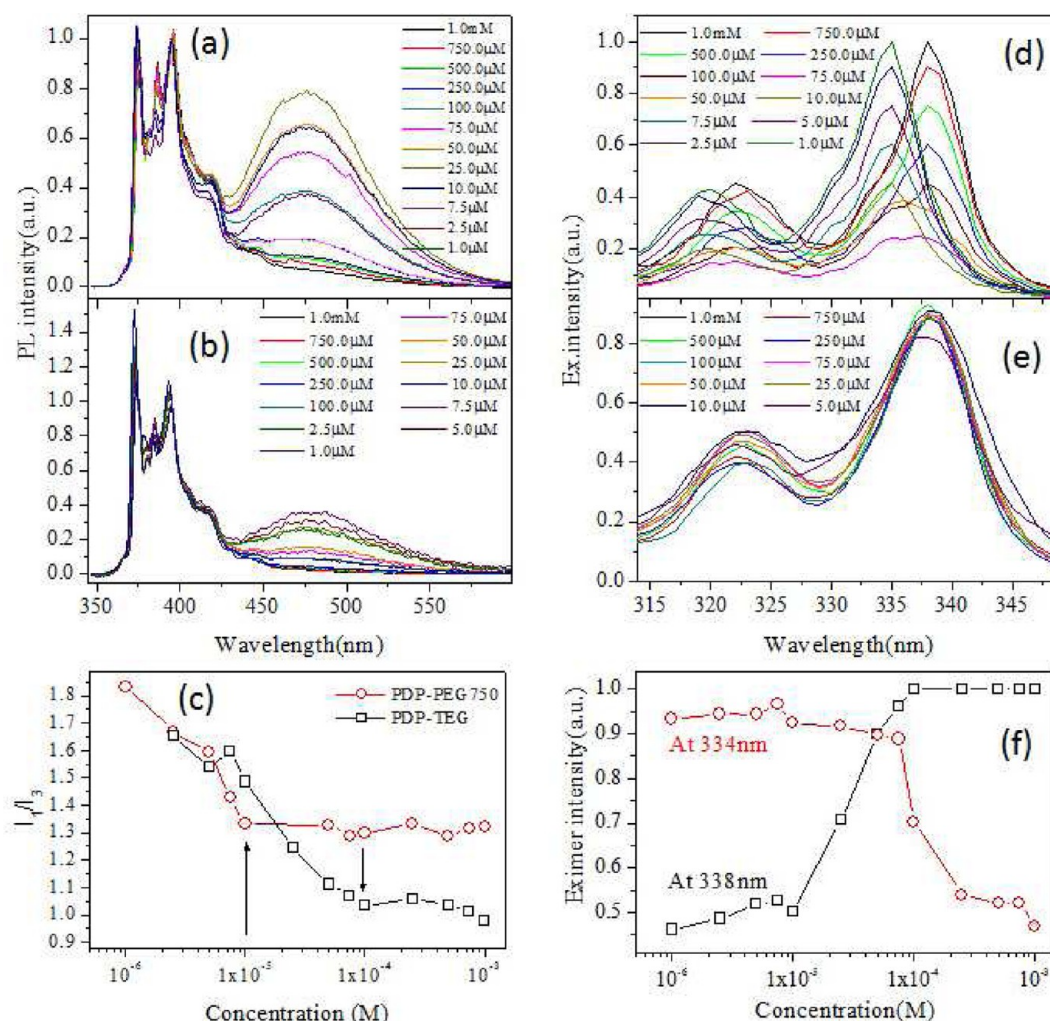


**Figure 5.** Emission spectra of pyrene at various concentrations of PDP-TEG (a) and PDP-PEG-750 (b) in PBS (excited at 337 nm). Plot of  $I_1/I_3$  versus the concentration of blocks (c). Excitation spectra of pyrene collected at monomer (d) and excimer emission (e) at various concentrations of PDP-TEG. Plots of excimer intensity versus the concentration of PDP-TEG (f).

from the enthalpies that the PDP-PEG-750 block has much higher enthalpies than their individual counterparts: PDP-acid and PEG-750 (see Table ST-2, Supporting Information). This provides direct evidence for the strong packing of diblocks via cooperative structural effects which lacked in their individual hydrophilic or hydrophobic parts alone. The strong intermolecular interaction in PDP-PEG-750 blocks produced a larger diblock membrane (8 times bigger in size) which further underwent inward invagination to produce MVBs as noticed in the biological cell membranes. On the other hand, the shorter hydrophilic content (PDP-TEG) produced a small and loosely packed membrane which preferred outward budding to form SUVs (as seen in many synthetic examples). Thus, a very good correlation between the theory and experimental results was established in the mechanistic aspects of SUVs and MVBs. The above studies revealed that strong unilamellar packing was essential for synthetic membranes to form MVBs. PDP-PEG-750 is a unique biomimicking synthetic block which produced exclusively MVBs through the inward invagination mechanism.

Fluorophore encapsulations provide direct evidence for mechanistic aspects of vesicle formation in water.<sup>18</sup> Pyrene was chosen as a fluorophore for the above purpose because of its well-known emission characteristics and its preferential occupation only at the hydrophobic layer of the vesicles.

Pyrene encapsulation resembles the hydrophobic drug loading in vesicles for therapeutics, and therefore, the encapsulation studies in the synthetic MVBs might provide insight into the MVB formation mechanism as well as their potential future applications. The concentration of pyrene was fixed as 0.6  $\mu$ M, and the concentrations of the A–B diblocks were varied from  $10^{-3}$  to  $10^{-6}$  M in water.<sup>19</sup> The emission spectra of blocks are shown in Figure 5a and b. PDP-TEG showed sharp emission peaks with respect to its monomer emission (360–420 nm) and additionally a broad excimer emission with maxima at 475 nm.<sup>18a,b</sup> The emission spectra of PDP-PEG-750 also showed the formation of excimer; however, the intensity was relatively less.

In general, pyrene does not form excimer at 0.6  $\mu$ M, since all molecules are completely isolated in water at this low probe concentration.<sup>18d,c</sup> Therefore, the appearance of excimer in the presence of A–B diblocks (in water) was direct evidence for the encapsulation of pyrene molecules in the self-organized structure. The  $I_1/I_3$  ratio of the monomer emission peaks was plotted against the concentration of the A–B diblocks (see Figure 5c). The  $I_1/I_3$  values were obtained in the range of  $1 < I_1/I_3 < 1.5$ , which indicated the encapsulation of pyrenes in the hydrophobic layer of the vesicles.<sup>19</sup> The break point in the  $I_1/I_3$  plots was the direct measure of their critical vesicular

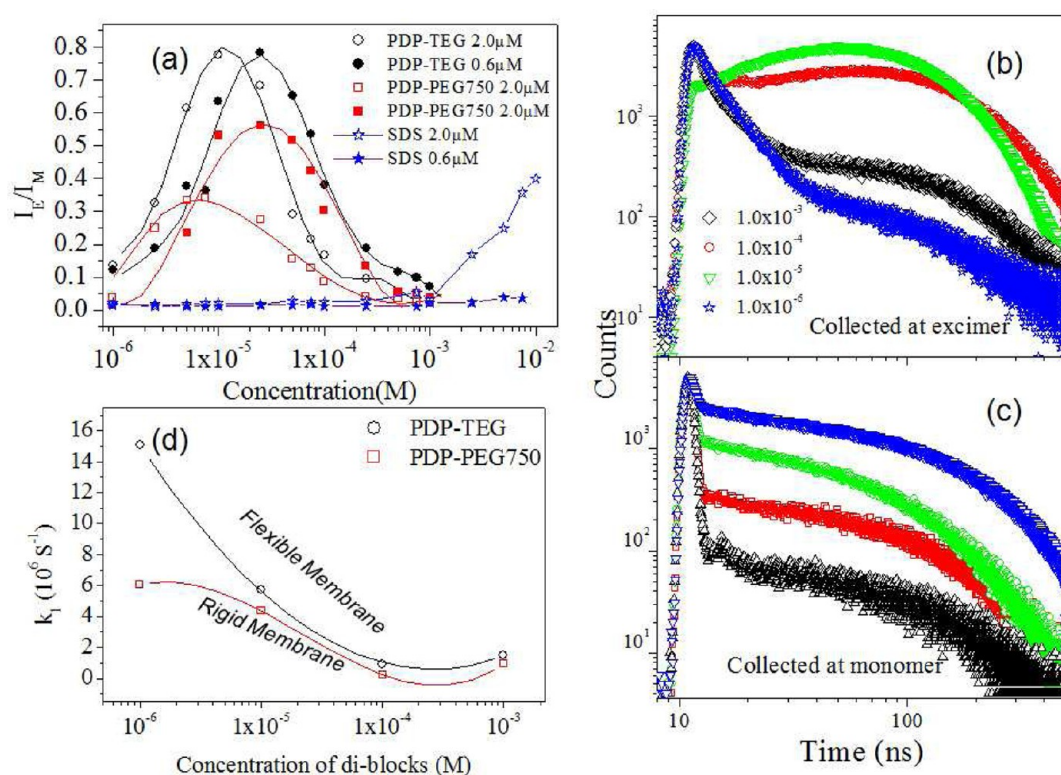


**Figure 6.** Plot of  $I_E/I_M$  versus the concentration of the diblocks and SDS (a). TCSPC fluorescent decay profiles of pyrene collected at excimer (b) and monomer (c) emission (excited with 339 nm LED laser source). Plots of excimer formation rate constant ( $k_1$ ) versus the concentration of the diblocks (d).

concentration (CVC), and the CVCs of the PDP-TEG and PDP-PEG-750 were obtained as  $1.0 \times 10^{-4}$  and  $1.0 \times 10^{-5}$  M, respectively. Excitation spectra of the pyrene molecules collected at both monomer and excimer emission are shown in Figure 5d and e, respectively. In Figure 5d, two peaks appeared at 334 and 338 nm which were characteristic of pyrene monomer absorption in the hydrophilic and hydrophobic environment, respectively.<sup>18d</sup> The excitation spectra shifted toward higher wavelength with the increase in the concentration of the diblock and also showed a clear isosbestic point at 336 nm. This confirmed the encapsulation of more pyrene molecules in the hydrophobic layer of the diblock membrane with an increase in the diblock concentration in water. A similar observation was also found for the pyrene encapsulation in PDP-PEG-750 blocks (see SF-10 and SF-11, Supporting Information). The plots of excitation intensity at 334 and 338 nm versus the concentration of the blocks (see Figure 5f) showed break points at  $1.0 \times 10^{-4}$  and  $1.0 \times 10^{-5}$  M for PDP-TEG and PDP-PEG-750, respectively. These break points were exactly the same as that of the CVC values obtained on the basis of the  $I_1/I_3$  ratio (see Figure 5c). The 1 order of magnitude difference in CVC values among the diblocks confirmed that the molecular self-organization of PDP-PEG-750 block ( $10^{-5}$  M) was stronger compared to that of PDP-TEG ( $10^{-4}$  M). These results were in accordance with the trend observed in DSC data and theoretical calculation, which once again confirmed the need for strong interchain interactions in the diblock membranes for MVBs in synthetic macromolecules.

Dynamic excimers are formed between excited state monomer and ground state pyrene during the photoexcitation process. The excitation spectra collected at the excimer emission showed the absorption at 338 nm with respect to pyrene

monomer in ground state. This is the direct proof for the formation of pyrene dynamic excimer during their encapsulation in the hydrophobic layer of diblock membranes.<sup>18a</sup> The intensities of the dynamic excimer emission were found to be highly sensitive to the concentration of the AB blocks in the solution. The ratio of PL intensities of excimer to monomer ( $I_E/I_M$ ) was plotted against the concentration of the diblocks and shown in Figure 6a. The plots showed an unusual non-linear trend with the concentration of AB diblocks in water. The intensity of the dynamic excimer emission initially increased with the increase in the diblock concentration, reached a maximum, and then decreased with further increase in diblock concentration. The magnitude of the intensity ratio (in Y-axis) was much higher for PDP-TEG blocks compared to that of its long PEG-chain block (PDP-PEG-750). This confirmed that the SUV formation (from PDP-TEG) was accompanied by strong pyrene excimer formation compared to that of the MVBs (from PDP-PEG-750). The comparison of  $I_E/I_M$  plots in Figures 6a and 5c (also Figure 5f) indicated that both the enhancement in the pyrene dynamic excimer formation and also its disappearance occurred much below the CVC of the diblocks. To prove this unusual excimer formation of pyrene in the vesicular structure, control experiments were carried out for pyrene encapsulation in sodium dodecyl sulfate (SDS) in PBS under identical conditions. Two pyrene concentrations (0.6 and 2.0  $\mu$ M) were chosen for the encapsulation studies in SDS in PBS to determine their  $I_1/I_3$  values with variable slit widths of 1.0, 0.8, and 0.5 nm (see plots in SF-12, Supporting Information). For 0.6  $\mu$ M pyrene,  $I_1/I_3$  values were obtained as  $I_1/I_3 = 1.5$  below CMC and  $I_1/I_3 = 1.1$  above CMC.<sup>18c</sup> At higher pyrene concentration (2.0  $\mu$ M),  $I_1/I_3$  values were obtained as  $I_1/I_3 = 1.8$  below CMC and  $I_1/I_3 = 1.2$  above CMC.<sup>20</sup>



Table 1. Fluorescence Decay Lifetime Data for PDP-TEG Block<sup>a</sup>

concentration of A–B diblock (M)	collected at excimer emission				$A_{E-}/A_{E+}$	collected at monomer emission		
	$\tau_1$ (ns)	$\tau_2$ (ns)	$\tau_3$ (ns)	$\chi^2$		$\tau_1$ (ns)	$\tau_2$ (ns)	$\chi^2$
$1.0 \times 10^{-3}$	0.9 (0.01)	4.6 (0.14)	157.0 (0.85)	1.16	0	0.003 (100)	112 (0.0)	1.17
$1.0 \times 10^{-4}$	2.2 (0.01)	41.0 (−0.25)	121.0 (0.99)	1.2	−0.25	19.7 (12.0)	120.0 (88.0)	1.12
$1.0 \times 10^{-5}$	30.0 (−0.22)	51.2 (−0.03)	72.0 (1.00)	1.13	−0.25	5.98 (37.6)	135.0 (62.3)	1.08
$1.0 \times 10^{-6}$	1.3 (0.16)	5.8 (0.41)	104 (0.43)	1.09	0	9.73 (2.1)	138 (97.8)	1.07

<sup>a</sup>The values in parentheses correspond to the amplitude of the exponential decay times.

In order to compare the encapsulation ability of pyrene in the new diblocks with that of SDS, 2.0  $\mu\text{M}$  pyrene was also encapsulated in the PDP-TEG and PDP-PEG-750 and their data are given in SF-13 (Supporting Information). The  $I_1/I_3$  values in the diblocks increased with the decrease in slit widths, as seen in the case of SDS (see SF-13, Supporting Information). To compare the excimer formation ability of pyrene in SDS with that of the new diblocks, the  $I_E/I_M$  ratios were plotted for both 0.6 and 2.0  $\mu\text{M}$  pyrene encapsulation (see Figure 6a). At lower concentration (0.6  $\mu\text{M}$ ), the pyrene molecules did not form excimer in SDS (see SF-12, Supporting Information), whereas excimer formation was noticed above CMC for 2.0  $\mu\text{M}$  concentration of pyrene. On the other hand, the newly designed diblocks PDP-TEG and PDP-PEG-750 showed pyrene excimer formation for both 0.6 and 2.0  $\mu\text{M}$  pyrene encapsulation. Additionally, the excimer formation showed unusual a nonlinear trend concentration of the blocks much below their CVCs. The reason for this trend may be attributed to the variation in the self-organization behavior of vesicular structure and the encapsulation capabilities of newly designed renewable diblocks compared to that of the SDS micelles.

To further study these unusual excimer trends, fluorescent decay profiles of pyrene were investigated by TCSPC techniques. The fluorescent decay profiles were collected at both monomer emission (at 375 nm) and excimer emission (at 475 nm) using a nano-LED laser source with 339 nm excitation wavelength. Pyrene fluorescent decay profiles at different PDP-TEG concentrations (from  $10^{-3}$  to  $10^{-6}$  M) are shown in Figure 6b and c (see SF-14, Supporting Information, for PDP-PEG-750). The decay profiles were fitted by bi- or triexponential decay fits, and their lifetime data are shown in Table 1 (see Table ST-3 in the Supporting Information for PDP-PEG-750). The initial building up of the decay curve at  $1 \times 10^{-5}$  M is the typical nature of the dynamic pyrene excimer formation.<sup>21a,b</sup> The decay profile of pyrene collected at monomer emission (see Figure 6c) showed a drastic change with the increase in the AB diblock concentration in water. This trend was attributed to the self-quenching of pyrene monomers, while the diblock membranes approached toward the CVC.<sup>21c</sup> Hence, the encapsulation of pyrene molecules in the hydrophobic layer of the diblock membrane occurred in a stepwise manner which was primarily controlled by self-organization of A–B diblocks in water. Although the excimer decay appeared to show a pronounced rise time, it seemed that the decays did not go down to zero at  $t = 0$ , which was a condition for excimer formation by diffusion. All excimer decays showed a short decay time observed often when pyrene aggregates were present, but at diblock concentrations of  $10^{-5}$  and  $10^{-4}$  M where pyrene was concentrated in a few hydrophobic domains, excimer was also formed by diffusion.<sup>18a</sup> This was demonstrated in Table 1 (also ST-3, Supporting Information) by normalizing the pre-exponential factors and calculating the  $A_{E-}/A_{E+}$  ratios where the ratio of the sum of the negative pre-exponential factors

divided by that of the positive pre-exponential factors, namely, the  $A_{E-}/A_{E+}$  ratio. The monomer decays showed a very short decay time ( $\tau_1 < 0.1$  ns) due to residual light scattering. It is worth noting that longer decay times were obtained for the monomer and excimer decays for the PDP-PEG750 samples. Long decay times indicate that quenching of pyrene by oxygen in the air was hindered in the tightly packed PDP-PEG750 vesicle membranes.

In order to explain the trend in the  $I_E/I_M$  ratio of pyrene chromophore in the SUVs and MVBs (in Figure 6a), the models developed by Cuniberti et al.<sup>22</sup> and Duhamel and co-workers<sup>23</sup> for pyrene labeled polymers were utilized. The  $I_E/I_M$  ratio was correlated to excimer formation parameters, as shown in eq 4:

$$I_E/I_M = \kappa[\phi_E^\circ/\phi_M^\circ]\tau_M k_1 [\text{Py}]_{\text{loc}} \quad (4)$$

where  $\kappa$  is a constant that depends on the geometry and sensitivity of the spectrofluorometer,  $\phi_E^\circ$  and  $\phi_M^\circ$  are the fluorescence quantum yields of the pyrene monomer and excimer, respectively, and  $\tau_M$  is the natural lifetime of the pyrene monomer. The other two parameters  $k_1$  and  $[\text{Py}]_{\text{loc}}$  represent the rate constant of excimer formation and the local pyrene concentration, respectively.<sup>23b</sup> Since the parameters  $\kappa$ ,  $\phi_E^\circ$ ,  $\phi_M^\circ$ , and  $\tau_M$  are constants and do not vary with the types of the amphiphiles (either PDP-TEG and PDP-PEG-750), it may be assumed that the trend in the  $I_E/I_M$  ratio in Figure 6a was directly influenced by  $k_1$  and  $[\text{Py}]_{\text{loc}}$ .<sup>23b</sup> As illustrated by Duhamel and co-workers, the  $k_1$  values could be experimentally determined by the expression  $k_1 = \{1/\langle\tau\rangle\} - \{1/\tau_M\}$ , where  $\langle\tau\rangle = \sum a_i \tau_i / \sum a_i$  corresponds to the number average lifetime for those pyrenes form excimer via diffusion.<sup>24</sup> The rate constant  $k_1$  for the excimer formation was calculated on the basis of excimer lifetimes (see Table 1 and ST-3, Supporting Information) and using the pyrene monomer lifetime,  $\tau_M = 168$  ns, as reported earlier.<sup>18c</sup> The excimer rate constant values are given in the Tables ST-4 and ST5 (Supporting Information).

The excimer formation rate constant  $k_1$  was plotted against the concentration of the PDP-TEG and PDP-PEG-750 and shown in Figure 6d. Two observations are very clear from these plots. First, the excimer rate constants decreased with the increase in the diblock concentration. This trend was attributed to the hindrance caused for the free diffusion of pyrene monomer by diblocks. Second, at low diblock concentration (below  $10^{-5}$  M), the excimer rate constant for the PDP-TEG was found to be almost 2 times higher than that of PDP-PEG-750. This was attributed to the difference in the rigidity of the diblock membranes. Typically, the rigid backbone is tightly packed and expected to hinder the diffusion of the pyrene monomers in the hydrophobic vesicular layer. The PDP-PEG-750 was found to be much more rigid compared to the PDP-TEG (evident from DSC data, ST2, Supporting Information), and therefore, the more rigid polymer chains provide less possibility for the pyrene monomer diffusion in the encapsulated



membrane layer. The decrease in the diffusion of excited state pyrene hampered the excimer formation which indirectly affects the reduction in the excimer formation rate constant. The MVBs produced by the rigid block PDP-PEG-750 showed feeble pyrene excimer emission due to the lesser probability for the overlap of the excited pyrene with ground state monomers. On the other hand, in the more flexible PDP-TEG block (produced SUVs), the excimer formation was promoted by the free diffusion of pyrene molecules. Hence, the larger variation in extent of  $I_E/I_M$  ratio ( $Y$ -axis) at lower diblock concentrations in Figure 6a was directly controlled by the rigidity of the diblock membranes. It is also important to mention that the  $I_E/I_M$  ratio (in eq 4) was also influenced by the local pyrene concentration  $[Py]_{loc}$ . Since the surface areas of the MVBs were 8 times higher than those of SUVs (see Figure 4), one may anticipate that more pyrene molecules could be accommodated in the MVBs compared to the latter. To check this hypothesis, a higher amount of pyrene was encapsulated ( $2.0 \mu\text{M}$ ) in both the diblocks of SUVs and MVBs (see excimer peaks in SF-15, Supporting Information). The  $I_E/I_M$  ratio did not show any major changes in the PDP-TEG (other than little maxima shift toward the lower concentration) which was attributed to saturation of pyrene loading in the small vesicular membranes (SUVs). Interestingly, the  $I_E/I_M$  ratio increased almost twice in PDP-PEG-750 with increase in the loading of pyrene from 0.6 to  $2.0 \mu\text{M}$  in the feed. With increase in the pyrene concentration in the feed (0.6 and  $2.0 \mu\text{M}$ ), the  $[Py]_{loc}$  concentration was also expected to increase in the vesicular membrane. Hence, the twice the increase in the  $I_E/I_M$  ratio in PDP-PEG-750 at higher pyrene incorporation may be attributed to the increase in the  $[Py]_{loc}$  concentration in the vesicular structure. However, the nonavailability of theoretical model and experimental techniques hampered the exact determination of  $[Py]_{loc}$ . Nevertheless, in the present investigation, the differences in the encapsulation capabilities of pyrene molecules in SUVs or MVBs were demonstrated very well using detailed photophysical studies. These studies revealed that the rigid diblock membrane PDP-PEG-750 (mother of MVBs) encapsulates pyrene molecules uniformly throughout the larger hydrophobic layer. This observation could be very useful for encapsulation of hydrophobic guest molecules like pyrene (or drugs) in MVBs for future applications in loading and delivering water insoluble polyaromatic drug molecules for therapeutics such as polymer based drug deliveries.

## CONCLUSION AND PATH FORWARD

In conclusion, new classes of AB diblock amphiphilic copolymers based on renewable resource hydrophobic unit and different hydrophilic PEG content were designed for mimicking MVBs in synthetic macromolecules. The rigid hydrophobic units formed very stable unilamellar structures through interdigitation of alkyl tails which was further confirmed by single crystal structures. PEG chain length in the diblock played a crucial role in determining the extent of the bilayer formation in water. The longer PEG-750 chain induced strong interchain packing in the diblock membrane, as a result of which they underwent inward curvature to form stomatocytes. The stomatocytes invaginated to produce MVBs containing 10 intraluminal vesicles of 45–50 nm in diameter. Diblocks with short hydrophilic units produced smaller membranes which seeded for SUVs via vesicular fission pathways. Theoretical models were adopted to determine the structural parameters such as relative volume ( $\nu_e$ ) and reduced

area difference ( $\Delta a_0$ ), and very good correlation between the theory and experimental results was obtained. The difference in the diblock molecular self-organization was further confirmed by the DSC analysis. The critical vesicular association (CVC) of the MVBs was found to be much lower ( $10^{-5} \text{ M}$ ) compared to that of the SUVs ( $10^{-4} \text{ M}$ ). Pyrene encapsulation studies showed an unusual nonlinear trend in the dynamic excimer formation of the self-organized diblock membrane. Controlled experiments were carried out using SDS to trace the factors which direct the vesicular membrane formation and their encapsulation capabilities of custom designed renewable resource diblocks. MVBs were found to be very unique in that rigid aromatic molecules could be encapsulated uniformly throughout the hydrophobic vesicular membrane. These synthetic MVBs might be very useful as vectors for administrating rigid drug molecules for therapeutic applications.

## EXPERIMENTAL SECTION

**Materials.** 3-Pentadecylphenol, 2-bromoethanol, succinicanhydride, triethylamine, triethyleneglycolmonomethylether, polyethylene glycol monomethylether ( $M_n = 750$ ), dicyclohexylcarbodiimide, and 4-dimethylamino pyridine were purchased from Aldrich chemicals. NaOH and all other reagents and solvents were purchased locally and purified following the standard procedures.

**General Procedures.**  $^1\text{H}$  NMR and  $^{13}\text{C}$  NMR spectra were recorded using a 400 MHz Jeol NMR spectrometer in  $\text{CDCl}_3$  containing a small amount of TMS as an internal standard. Infrared spectra were recorded using a Thermo-Scientific Nicolet 6700FT-IR spectrometer with the solid state in KBr. The mass of all the diblock polymers was confirmed by using the Applied Biosystems 4800 PLUS MALDI TOF/TOF analyzer. The purity of the diblock polymers were determined by gel permeation chromatography (GPC) using a Viscotek VE 1122 pump, ViscotekVE 3580 RI detector, and Viscotek VE 3210 UV/vis detector in tetrahydrofuran (THF) using polystyrene as standards. The absorption and emission studies were done by a Perkin-Elmer Lambda 45 UV–visible spectrophotometer, and steady state fluorescence emission and excitation spectra were recorded using a Fluorolog HORIBA JOBIN VYON fluorescence spectrophotometer. The excitation spectra are collected at 395 and 476 nm (pyrene emission wavelength), and the emission spectra are recorded by exciting at the excitation maxima. The pyrene samples were purged with  $\text{N}_2$  gas for at least 15–20 min prior to photophysical experiments. The size determination of the diblock polymer solution is carried out by dynamic light scattering (DLS), using a Nano ZS-90 apparatus utilizing a 633 nm red laser from Malvern instruments. The reproducibility of the data was checked for at least three independent polymer solutions. Atomic force microscope images were recorded for drop cast samples using JPK instruments attached with Nanowizard-II setup. AFM is also attached with a Zeiss inverted optical microscope. TEM images were recorded using a Technai-300 instrument. Differential scanning calorimetry (DSC) measurements were performed on a TA Q20 differential scanning calorimeter (DSC) at heating and cooling rates of  $5.0 \text{ }^\circ\text{C}/\text{min}$ . Single crystals were subjected to data collection at 100 K on a Bruker APEX duo CCD-X-ray diffractometer equipped with graphite monochromated Mo K $\alpha$  radiation ( $\lambda = 0.71073 \text{ \AA}$ ). The frames were integrated with a Bruker APEX software package. The structures were solved by direct methods and refined

with a full matrix least-squares technique using SHELX S v97 programs.

**Synthesis of 2-(3-Pentadecylphenoxy)ethanol (1a).** Sodium hydroxide (3.5 g, 88.0 mmol) was dissolved in ethanol–water mixture (1:1 v/v, 100 mL) in a 250 mL flask and was purged with nitrogen for 10 min. 3-Pentadecylphenol (12.0 g, 40.0 mmol) was added into the reaction mixture, and the content was refluxed for 30 min at 100 °C. It was cooled, and then, freshly distilled 2-bromoethanol (6.4 g, 80 mmol) was added dropwise. The reaction mixture was then refluxed for 24 h under nitrogen atmosphere. It was poured into water (100 mL), extracted with ethyl acetate, and washed subsequently with 5% NaOH solution and brine. The organic layer was dried over anhydrous sodium sulfate, filtered, and evaporated to obtain pale yellow solid as product. It was purified by passing through a silica gel column of 60–120 mesh using 3% ethyl acetate in hexane as eluent. Yield = 7.6 g (55%). <sup>1</sup>H NMR (CDCl<sub>3</sub>, 400 MHz)  $\delta$ : 7.17 ppm (t, 1H, Ar–H), 6.75 ppm (m, 3H, Ar–H), 4.08 ppm (t, 2H, Ar–OCH<sub>2</sub>), 3.95 ppm (t, 2H, CH<sub>2</sub>–OH), 2.57 ppm (t, 2H, Ar–CH<sub>2</sub>), 1.6–0.88 ppm (m, 29H, aliphatic H). <sup>13</sup>C NMR (CDCl<sub>3</sub>, 100 MHz)  $\delta$ : 158.66, 144.87, 129.31, 121.42, 114.89, 111.51 (Ar–C), 66.07 (Ar–OCH<sub>2</sub>), 61.64 (CH<sub>2</sub>–OH), 36.11, 32.02, 31.50, 29.78, 29.62, 29.46, 22.80, 14.22. FT-IR (cm<sup>−1</sup>): 3369, 3293, 2912, 2848, 1593, 1457, 1357, 1264, 1172, 1087, 1047, 958, 898, 785, 697, 598. MALDI-TOF-MS: *m/z* calculated for C<sub>23</sub>H<sub>40</sub>O<sub>2</sub> (MW = 348.56): theoretical, 387.56; found, 387.19 (M<sup>+</sup> + K<sup>+</sup>).

**Synthesis of (E)-2-(3-(Pentadec-8-en-1-yl)phenoxy)-ethanol (1b).** Cardanol (10.0 g, 33.0 mmol) and 2-bromoethanol (6.2 g, 49.5 mmol) were reacted in the presence of NaOH (2.64 g, 66.0 mmol) in ethanol–water mixture (1:1 v/v, 100 mL) as described for 1a. It was purified by passing through a silica gel column of 60–120 mesh using 3% ethyl acetate in hexane as eluent. Yield = 6.0 g (53%). <sup>1</sup>H NMR (CDCl<sub>3</sub>, 400 MHz)  $\delta$ : 7.18 ppm (t, 1H, Ar–H), 6.79 ppm (m, 3H, Ar–H), 4.08 ppm (t, 2H, Ar–OCH<sub>2</sub>), 5.34 ppm (d, CH=CH), 3.96 ppm (t, 2H, CH<sub>2</sub>–OH), 2.57 ppm (t, 2H, Ar–CH<sub>2</sub>), 1.6–0.88 ppm (m, 29H, aliphatic H). <sup>13</sup>C NMR (CDCl<sub>3</sub>, 100 MHz)  $\delta$ : 158.66, 144.87, 129.31, 121.42, 114.89, 111.51 (Ar–C), 66.07 (Ar–OCH<sub>2</sub>), 61.64 (CH<sub>2</sub>–OH), 36.11, 32.02, 31.50, 29.78, 29.62, 29.46, 22.80, 14.22. FT-IR (cm<sup>−1</sup>): 3370, 2923, 2854, 1569, 1487, 1449, 1373, 1258, 1159, 1078, 1048, 964, 899, 874, 777, 725, 694, 609. MALDI-TOF-MS: *m/z* calculated for C<sub>23</sub>H<sub>38</sub>O<sub>2</sub> (MW = 346.55): theoretical, 385.55; found, 385.15 (M<sup>+</sup> + K<sup>+</sup>).

**Synthesis of 4-oxo-4-(2-(3-Pentadecylphenoxy)-ethoxy)butanoic acid (2a)-PDP-COOH.** Compound 1a (4.0 g, 11.4 mmol) and succinic anhydride (1.4 g, 13.8 mmol) were taken in dichloromethane (50 mL) in a 100 mL flask. Triethylamine (1.5 mL, 11.4 mmol) was added dropwise and the reaction started immediately followed by vigorous boiling. The reaction mixture was stirred at 30 °C for 24 h. It was poured in 100 mL of water and neutralized with 2N concentrated HCl (2 drops). The crude solid was filtered and further purified by crystallization from hot methanol. Yield = 3.3 g (64%). <sup>1</sup>H NMR (CDCl<sub>3</sub>, 400 MHz)  $\delta$ : 7.18 ppm (t, 1H, Ar–H), 6.78 ppm (m, 3H, Ar–H), 4.45 ppm (t, 2H, Ar–OCH<sub>2</sub>), 4.16 ppm (t, 2H, CH<sub>2</sub>–O), 2.68 ppm (s, 4H, CO–CH<sub>2</sub>–CH<sub>2</sub>), 2.56 ppm (t, 2H, Ar–CH<sub>2</sub>), 1.6–0.88 ppm (m, 29H, aliphatic H). <sup>13</sup>C NMR (CDCl<sub>3</sub>, 100 MHz)  $\delta$ : 177.82 (CO–OH), 172.11 (O–CO) 158.38, 144.75, 129.19, 121.38, 114.85, 111.41 (Ar–C), 65.63 (Ar–OCH<sub>2</sub>), 63.26 (CH<sub>2</sub>–O), 36.0, 31.91, 31.38, 29.67, 29.35, 28.77, 28.71, 22.68, 14.11. FT-IR (cm<sup>−1</sup>): 2918, 2848,

1738, 1700, 1581, 1454, 1396, 1293, 1233, 1172, 1081, 938, 864, 784, 687, 572. MALDI-TOF-MS: *m/z* calculated for C<sub>27</sub>H<sub>44</sub>O<sub>5</sub> (MW = 448.64): theoretical, 487.64; found, 487.17 (M<sup>+</sup> + K<sup>+</sup>).

**Synthesis of (E)-4-oxo-4-(2-(3-(Pentadec-8-en-1-yl)-phenoxy)ethoxy)butanoic Acid (2b)-CAR-COOH.** Compound 1b (6.0 g, 17.0 mmol) was reacted with succinic anhydride (2.1 g, 2.0 mmol), in the presence of Et<sub>3</sub>N (1.7 g, 17.3 mmol) in dichloromethane (60.0 mL) as described for 2a. It was purified by passing through a silica gel column of 60–120 mesh using 8% ethyl acetate in hexane as eluent. Yield = 4.0 g (52%). <sup>1</sup>H NMR (CDCl<sub>3</sub>, 400 MHz)  $\delta$ : 7.17 ppm (t, 1H, Ar–H), 6.79 ppm (m, 3H, Ar–H), 5.34 ppm (d, CH=CH), 4.46 ppm (t, 2H, Ar–OCH<sub>2</sub>), 4.16 ppm (t, 2H, CH<sub>2</sub>–O), 2.68 ppm (t, 2H, Ar–CH<sub>2</sub>), 2.56 ppm (t, 2H, Ar–CH<sub>2</sub>), 1.6–0.88 ppm (m, 29H, aliphatic H). <sup>13</sup>C NMR (CDCl<sub>3</sub>, 100 MHz)  $\delta$ : 178.04 (CO–OH), 172.13 (O–CO) 158.34, 144.64, 129.8, 129.15, 121.32, 114.81, 111.37 (Ar–C), 65.58 (Ar–OCH<sub>2</sub>), 63.22 (CH<sub>2</sub>–O), 35.93, 31.32, 29.67, 29.35, 29.26, 29.16, 28.79, 28.67, 27.15, 22.70, 14.07. FT-IR (cm<sup>−1</sup>): 2916, 2851, 1726, 1589, 1444, 1250, 1169, 1063, 966, 780, 691, 611. MALDI-TOF-MS: *m/z* calculated for C<sub>27</sub>H<sub>42</sub>O<sub>5</sub> (MW = 446.62): theoretical, 485.62; found, 485.16 (M<sup>+</sup> + Na<sup>+</sup>).

**Synthesis of 2-(2-(2-Methoxyethoxy)ethoxy)ethyl (2-(3-Pentadecylphenoxy)ethyl) Succinate (PDP-TEG).** Compound 2a (5.0 g, 11.1 mmol), triethylene glycol monomethyl ether (2.2 g, 13.3 mmol), and 4-dimethylamino pyridine (0.1 g, 1.1 mmol) were dissolved in dry dichloromethane (50 mL) under N<sub>2</sub> atmosphere. The reaction mixture was cooled and stirred at 5 °C for 10 min. To this ice-cooled mixture, dicyclohexylcarbodiimide (2.8 g, 13.3 mmol) was added and stirring was continued for 10 min at 5 °C. The reaction continued for 24 h at 25 °C under N<sub>2</sub> atmosphere. The solvent was evaporated, and the solid mass was dissolved in ethyl acetate (200 mL). The white precipitate of DCU obtained was filtered using a G3-sintered funnel. The filtrate was washed with water (200 mL), neutralized with 2N HCl (2 mL), washed with 5% Na<sub>2</sub>CO<sub>3</sub> solution (100 mL), and dried over anhydrous sodium sulfate. The solvent was evaporated to obtain a yellow liquid as a product. It was further purified by passing through a silica gel column using 25% ethyl acetate in hexane as eluent. Further, it was purified by dialysis against water using a semipermeable membrane (MWCO-1,000). Yield = 2.1 g (30%). <sup>1</sup>H NMR (CDCl<sub>3</sub>, 400 MHz)  $\delta$ : 7.18 ppm (t, 1H, Ar–H), 6.73 ppm (m, 3H, Ar–H), 4.44 ppm (t, 2H, Ar–OCH<sub>2</sub>), 4.24 ppm (t, 2H, O–CH<sub>2</sub>–CH<sub>2</sub>), 4.15 ppm (t, 2H, CH<sub>2</sub>–O), 3.38 ppm (s, 3H, O–CH<sub>3</sub>), 3.65 ppm (t, 8H, CH<sub>2</sub>–O–CH<sub>2</sub>), 3.56 ppm (t, 2H, CH<sub>2</sub>–OCH<sub>3</sub>), 2.66 ppm (s, 4H, CO–CH<sub>2</sub>–CH<sub>2</sub>), 2.58 ppm (t, 2H, Ar–CH<sub>2</sub>), 1.59–0.88 ppm (m, 29H, aliphatic H). <sup>13</sup>C NMR (CDCl<sub>3</sub>, 100 MHz)  $\delta$ : 172.22 (O–CO) 158.36, 144.70, 129.14, 121.31, 114.79, 111.37 (Ar–C), 71.85 (C–OCH<sub>3</sub>), 70.5–68.9 (O–CH<sub>2</sub>–CH<sub>2</sub>O), 65.6 (Ar–OCH<sub>2</sub>), 63.82 (CH<sub>2</sub>–O), 58.98 (O–CH<sub>3</sub>), 35.96, 31.87, 31.36, 29.64, 29.55, 29.47, 29.37, 29.31, 28.91, 22.64, 14.09. FT-IR (cm<sup>−1</sup>): 2920, 2857, 1738, 1588, 1451, 1351, 1253, 1149, 1104, 857, 784, 696, 572. MALDI-TOF-MS: *m/z* calculated for C<sub>34</sub>H<sub>58</sub>O<sub>8</sub> (MW = 594.82): theoretical, 617.82; found, 617.46 (M<sup>+</sup> + Na<sup>+</sup>).

**Synthesis of 2,5,8,11,14,17,20,23,26,29,32,35,38,41,44,47,50-Heptadeca-oxadopentacontan-52-yl(2-(3-pentadecylphenoxy)ethyl)succinate (PDP-PEG750).** Compound 2a (1.0 g, 2.2 mmol), polyethylene glycol monomethyl ether (M<sub>n</sub> = 750) (2.0 g, 2.6 mmol), and 4-dimethylamino pyridine (0.3 g, 0.2 mmol) were reacted with dicyclohexylcarbodiimide

(0.5 g, 2.6 mmol) as described for PDP-TEG. It was further purified by passing through a silica gel column using 20% methanol in dichloromethane as eluent. The product was repetitively washed with *n*-hexane to remove the unreacted PEG-750 and further purified by dialysis against water using a semipermeable membrane (MWCO-1,000). Yield = 1.5 g (35%).  $^1\text{H}$  NMR ( $\text{CDCl}_3$ , 400 MHz)  $\delta$ : 7.15 ppm (t, 1H, Ar-H), 6.69 ppm (m, 3H, Ar-H), 4.40 ppm (t, 2H, Ar-OCH<sub>2</sub>), 4.19 ppm (t, 2H, O-CH<sub>2</sub>-CH<sub>2</sub>), 4.12 ppm (t, 2H, CH<sub>2</sub>-O), 3.65–3.59 ppm (s, 32H, CH<sub>2</sub>-O-CH<sub>2</sub>), 3.34 ppm (s, 3H, O-CH<sub>3</sub>), 2.64 ppm (s, 4H, CO-CH<sub>2</sub>-CH<sub>2</sub>), 2.53 ppm (t, 2H, Ar-CH<sub>2</sub>), 1.55–0.88 ppm (m, 29H, aliphatic H).  $^{13}\text{C}$  NMR ( $\text{CDCl}_3$ , 100 MHz)  $\delta$ : 172.25 (O-CO) 158.39, 144.73, 129.18, 121.32, 114.80, 111.41 (Ar-C), 71.88 (C-OCH<sub>3</sub>), 70.5–69.0 (O-CH<sub>2</sub>-CH<sub>2</sub>O), 65.64 (Ar-OCH<sub>2</sub>), 63.85 (CH<sub>2</sub>-O), 59.01 (O-CH<sub>3</sub>), 31.94, 31.47, 30.08, 29.67, 29.58, 29.34, 22.67, 14.10. FT-IR ( $\text{cm}^{-1}$ ): 2920, 2857, 1735, 1650, 1595, 1457, 1349, 1247, 1096, 947, 853, 697, 567. MALDI-TOF-MS:  $m/z$  calculated for  $\text{C}_{62}\text{H}_{114}\text{O}_{22}$ : theoretical, 1233; found, 1234.07 ( $\text{M}^+ + \text{Na}^+$ ).

**Synthesis of (E)-2,5,8,11,14,17,20,23,26,29,32,35,38,41,44,47,50-Heptadecaaxadopentacontan-52-yl(2-(3-(penta-dec-8-en-1-yl)phenoxy)ethyl) Succinate (CAR-PEG750).** Compound **2b** (6.0 g, 17.0 mmol), polyethyleneglycolmonomethyl ether ( $M_n = 750$ , 12.1 g, 16.0 mmol), and 4-dimethylamino pyridine (0.2 g, 1.3 mmol) were reacted with dicyclohexylcarbodiimide (3.3 g, 16 mmol) as described for PDP-TEG. It was further purified by passing through a silica gel column using 15% methanol in dichloromethane as eluent. The crude product was repetitively washed with *n*-hexane to remove the unreacted PEG-750 and further purified by dialysis against water using a semipermeable membrane (MWCO-1,000). Yield = 2.1 g (13%).  $^1\text{H}$  NMR ( $\text{CDCl}_3$ , 400 MHz)  $\delta$ : 7.14 ppm (t, 1H, Ar-H), 6.74 ppm (m, 3H, Ar-H), 5.28 ppm (d, CH=CH), 4.39 ppm (t, 2H, Ar-OCH<sub>2</sub>), 4.19 ppm (t, 2H, O-CH<sub>2</sub>-CH<sub>2</sub>), 4.08 ppm (t, 2H, CH<sub>2</sub>-O), 3.59 ppm (s, 32H, CH<sub>2</sub>-O-CH<sub>2</sub>), 3.32 ppm (s, 3H, O-CH<sub>3</sub>), 2.62 ppm (s, 4H, CO-CH<sub>2</sub>-CH<sub>2</sub>), 2.50 ppm (t, 2H, Ar-CH<sub>2</sub>), 1.55–0.88 ppm (m, 29H, aliphatic H).  $^{13}\text{C}$  NMR ( $\text{CDCl}_3$ , 100 MHz)  $\delta$ : 172.25 (O-CO) 158.39, 144.73, 129.18, 121.32, 114.80, 111.39 (Ar-C), 71.88 (C-OCH<sub>3</sub>), 70.5–69.0 (O-CH<sub>2</sub>-CH<sub>2</sub>O), 65.64 (Ar-OCH<sub>2</sub>), 63.85 (CH<sub>2</sub>-O), 59.01 (O-CH<sub>3</sub>), 31.94, 31.47, 30.08, 29.67, 29.58, 29.34, 22.67, 14.10. FT-IR ( $\text{cm}^{-1}$ ): 2928, 2866, 1738, 1657, 1593, 1537, 1454, 1347, 1244, 1093, 947, 849, 792, 696, 568. MALDI-TOF-MS:  $m/z$  calculated for  $\text{C}_{62}\text{H}_{112}\text{O}_{22}$ : theoretical, 1143; found, 1143.99 ( $\text{M}^+ + \text{Na}^+$ ).

## ■ ASSOCIATED CONTENT

### ■ Supporting Information

Crystallographic images, unit cells, calculation of relative volume, reduced area difference, DLS data, DSC traces, emission spectra and TCSPC lifetime plots, GPC plots, and  $^1\text{H}$  NMR,  $^{13}\text{C}$  NMR, and MALDI spectra. The crystallographic information file (cif) of the single crystal structure for compound **2a** was already deposited to Cambridge Crystallographic data center. CCDC-846783 contains the supplementary crystallographic data for this paper. This material is available free of charge via the Internet at <http://pubs.acs.org>.

## ■ AUTHOR INFORMATION

### Corresponding Author

\*E-mail: jayakannan@iiserpune.ac.in. Fax: +91-20-2590 8186.

## Notes

The authors declare no competing financial interest.

## ■ ACKNOWLEDGMENTS

The authors are thankful for the research grant from Department of Science and Technology (DST), New Delhi, India, under nanomission initiative project SR/NM/NS-42/2009 and SERC-scheme under the project SR/S1/OC-54/2009. S.K. thanks CSIR, India, for the Ph.D. research fellowship.

## ■ REFERENCES

- (1) Gibbings, D. J.; Ciaudo, C.; Erhardt, M.; Voinnet, O. *Nat. Cell Biol.* **2009**, *11*, 1143–1149.
- (2) Raiborg, C.; Rusten, T. E.; Stenmark, H. *Curr. Opin. Cell Biol.* **2003**, *15*, 446–455.
- (3) Hurley, J. H.; Boura, E.; Carlson, L. A.; Rozycki, B. *Cell* **2010**, *143*, 875–887.
- (4) Davies, B. A.; Lee, J. R. E.; Oestreich, A. J.; Katzmman, D. J. *Chem. Rev.* **2009**, *109*, 1575–1586.
- (5) Tran, J. H.; Chen, C. J.; Emr, S.; Schekman, R. *Proc. Natl. Acad. Sci. U.S.A.* **2009**, *106*, 17395–17400.
- (6) Wollert, T.; Hurley, J. H. *Nature* **2010**, *464*, 864–869.
- (7) Babst, M. *Curr. Opin. Cell Biol.* **2011**, *23*, 452–457.
- (8) (a) Ludwig, A. K.; Geibel, B. *Int. J. Biochem. Cell Biol.* **2012**, *44*, 11–15. (b) Lassic, D. D. *Biochem. J.* **1988**, *256*, 1–11.
- (9) (a) Murakami, Y.; Nakano, A.; Fukuya, K. *J. Am. Chem. Soc.* **1980**, *102*, 4253–4254. (b) Boyer, C.; Zasadzinski, J. A. *ACS Nano* **2007**, *3*, 176–182. (c) Richard, A.; Marchi-Artzner, V.; Lalloz, M.-N.; Brienne, M.-J.; Artzner, F.; Gulik-Krzywicki, T.; Guedeau-Boudeville, M.-A.; Lehn, J.-M. *Proc. Natl. Acad. Sci. U.S.A.* **2004**, *101*, 15279–15284. (d) Jeon, Y. J.; Bharadwaj, P. K.; Choi, S. W.; Lee, J. W.; Kim, K. *Angew. Chem., Int. Ed.* **2002**, *41*, 4474–4476. (e) Nalluri, S. K. M.; Ravoo, B. J. *Angew. Chem., Int. Ed.* **2010**, *49*, 5371–5374. (f) Azagarsamy, M. A.; Sokkalingam, P.; Thayumanavan, S. *J. Am. Chem. Soc.* **2009**, *131*, 14184–14185. (g) Tao, W.; Liu, Y.; Jiang, B.; Yu, S.; Huang, W.; Zhou, Y.; Yan, D. *J. Am. Chem. Soc.* **2012**, *134*, 762–764.
- (10) (a) Balachandran, V. S.; Jadhav, S. R.; Pradhan, P.; Carlo, S. D.; John, G. *Angew. Chem., Int. Ed.* **2010**, *49*, 9509–9512. (b) Koback, M. A.; Keating, C. D. *J. Am. Chem. Soc.* **2011**, *133*, 9545–9555. (c) Meledandri, C. J.; Perlo, J.; Farrher, E.; Brougham, D. F.; Anordor, E. *J. Phys. Chem. B* **2009**, *113*, 15532–15540. (d) Mahabir, S.; Wan, W.; Katsaras, J.; Nieh, M. P. *J. Phys. Chem. B* **2010**, *114*, 5729–5735.
- (11) (a) Tanaka, T.; Yamazaki, M. *Langmuir* **2004**, *20*, 5160–5164. (b) Zhou, Y.; Yan, D. *Angew. Chem., Int. Ed.* **2005**, *44*, 3223–3226. (c) Cans, A.-S.; Andes-Koback, M.; Keating, C. D. *J. Am. Chem. Soc.* **2008**, *130*, 7400–7406.
- (12) (a) Ghosh, S.; Reches, M.; Gazit, E.; Verma, S. *Angew. Chem., Int. Ed.* **2007**, *46*, 2002–2004. (b) Ghosh, S.; Verma, S. *Chem.—Eur. J.* **2008**, *14*, 1415–1419.
- (13) (a) Barbetta, A.; Pucci, C.; Tardani, F.; Andreozzi, P.; Mesa, C. L. *J. Phys. Chem. B* **2011**, *115*, 12751–12758. (b) Scholtysek, P.; Achilles, A.; Hoffmann, C. V.; Lechner, B. D.; Meister, A.; Tschierske, C.; Saalwachter, K.; Edwards, K.; Blume, A. *J. Phys. Chem. B* **2012**, *116*, 4871–4878. (c) Smith, A. E.; Xu, X.; York, S. E. K.; Savin, D. A.; McCormick, C. L. *Macromolecules* **2010**, *43*, 1210–1217. (d) Sun, V. Z.; Deming, T. J.; Kamei, D. T. *Biomacromolecules* **2011**, *12*, 10–13. (e) Chen, Z. X.; Su, X. X.; Deng, S. P. *J. Phys. Chem. B* **2011**, *115*, 1798–1806.
- (14) (a) Chiu, H. C.; Lin, Y. W.; Huang, Y. F.; Chuang, C. K.; Chern, C. S. *Angew. Chem., Int. Ed.* **2008**, *47*, 1875–1878. (b) Gao, W. P.; Bai, Y.; Chen, E. Q.; Li, Z. C.; Han, B. Y.; Yang, W. T.; Zhou, Q. F. *Macromolecules* **2006**, *39*, 4894–4898. (c) Lorenceau, E.; Utada, A. S.; Link, D. R.; Cristobal, G.; Joniact, M.; Weitz, D. A. *Langmuir* **2005**, *21*, 9183–9186. (d) Sofou, S.; Kappel, B. J.; Jaggi, J. S.; McDevitt, M. R.; Scheinberg, D. A.; Sgouros, G. *Bioconjugate Chem.* **2007**, *18*, 2061–2067. (e) Hosoda, K.; Sunami, T.; Kazuta, Y.; Matsuura, T.; Suzuki, H.; Yomo, T. *Langmuir* **2008**, *24*, 13540–13548. (f) Sagar, G. H.;



- Tiwari, M. D.; Bellare, J. R. *J. Phys. Chem. B* **2010**, *114*, 10010–10016.
- (g) Pozzi, G.; Birault, V.; Werner, B.; Dannenmuller, O.; Nakatani, Y.; Ourisson, G.; Terakawa, S. *Angew. Chem., Int. Ed. Engl.* **1996**, *35*, 177–180. (h) Meeuwissen, S. A.; Kim, K. T.; Chen, Y.; Pochan, D. J.; van Hest, J. C. M. *Angew. Chem., Int. Ed.* **2011**, *50*, 7070–7073.
- (15) Jin, Q.; Liu, G.; Liu, X.; Ji, J. *Soft Matter* **2010**, *6*, 5589–5595.
- (16) (a) Smith, L. A.; Hammond, R. B.; Roberts, K. J.; Machin, D.; McLeod, G. *J. Mol. Struct.* **2000**, *554*, 173–182. (b) Smith, L. A.; Thomson, G. B.; Roberts, K. J.; Machin, D.; McLeod, G. *Cryst. Growth Des.* **2005**, *5*, 2164–2172.
- (17) (a) Antoneitti, M.; Forster, S. *Adv. Mater.* **2003**, *15*, 1323–1333. (b) Seifert, U.; Berndt, K.; Lipowsky, R. *Phys. Rev. A* **1991**, *44*, 1182–1202. (c) Mui, B. L. S.; Dobereiner, H. G.; Madden, T. D.; Cullis, P. R. *Biophys. J.* **1995**, *69*, 930–941. (d) Svetina, S.; Zeks, B. *Eur. Biophys. J.* **1989**, *17*, 101–111.
- (18) (a) Winnik, F. M. *Chem. Rev.* **1993**, *93*, 587–614. (b) Baig, C. K.; Duhamel, J.; Fung, S. Y.; Bezaire, J.; Chen, P. *J. Am. Chem. Soc.* **2004**, *126*, 7522–7532. (c) Kalyanasundaram, K.; Thomas, J. K. *J. Am. Chem. Soc.* **1977**, *99*, 2039–2044. (d) Kawaguchi, S.; Yekta, A.; Duhamel, J.; Winnik, M. A. *J. Phys. Chem.* **1994**, *98*, 7891–7898. (e) Duhamel, J.; Yekta, A.; Winnik, M. A. *J. Phys. Chem.* **1993**, *97*, 2759–2763.
- (19) (a) Changez, Kang, M.; G., N.; Lee, C. H.; Lee, J. S. *Small* **2010**, *6*, 63–68. (b) De Maria, P.; Fontana, A.; Siani, G.; D'Aurizio, E.; Cerichelli, G.; Chiarini, M.; Angelini, G.; Gasbarri, C. *Colloids Surf., B* **2011**, *87*, 73. (c) Delamplé, M.; Jerome, F.; Barrault, J.; Douliez, J.-P. *Green Chem.* **2011**, *13*, 64.
- (20) (a) Dong, D. C.; Winnik, M. A. *Photochem. Photobiol.* **1982**, *35*, 17–21. (b) Dong, D. C.; Winnik, M. A. *Can. J. Chem.* **1984**, *62*, 2560–2565.
- (21) (a) Costa, T.; Melo, J. S. S. D.; Castro, C. S.; Gago, S.; Pillinger, M.; Goncalves, I. S. *J. Phys. Chem. B* **2010**, *114*, 12439–12447. (b) Kaushlendra, K.; Deepak, V. D.; Asha, S. K. *J. Polym. Sci., Part A: Polym. Chem.* **2011**, *49*, 1678–1690. (c) Vanderkooi, J. M.; Callis, J. B. *Biochemistry* **1974**, *19*, 4000–4006.
- (22) Cuniberti, C.; Perico, A. *Eur. Polym. J.* **1980**, *16*, 887–893.
- (23) (a) Duhamel, J. *Acc. Chem. Res.* **2006**, *39*, 953–960. (b) Ingratta, M.; Hollinger, J.; Duhamel, J. *J. Am. Chem. Soc.* **2008**, *130*, 9420–9428. (c) Yip, J.; Duhamel, J.; Qiu, X. P.; Winnik, F. M. *Can. J. Chem.* **2011**, *89*, 163–172. (d) Teertstra, S. J.; Lin, W. Y.; Gautheir, M.; Ingratta, M.; Duhamel, J. *Polymer* **2009**, *50*, 5456–5466.
- (24) (a) Ingratta, M.; Duhamel, J. *J. Phys. Chem. B* **2008**, *112*, 9209–9218. (b) Yip, J.; Duhamel, J.; Bahun, G. J.; Adronov, A. *J. Phys. Chem. B* **2010**, *114*, 10254–10265.